Analyses of Backward Erosion Progression Rates from Small-Scale Flume Experiments

B. A. Robbins, P.E., M.ASCE[1]; A. M. Montalvo-Bartolomei, P.E., M.ASCE[2]; and D. V. Griffiths, P.E., Dist.M.ASCE[3]

Abstract: Backward erosion piping is a leading cause of levee failures, second only to overtopping, and is therefore of great concern to engineers involved in flood control. Backward erosion piping refers to a process by which shallow erosion channels propagate upstream through foundation sands beneath water-retaining structures. If the erosion channels reach the upstream source of water, the channels rapidly enlarge, which can ultimately lead to collapse of the structure. Observations from the Mississippi River indicate that most erosion incidents do not lead to failure. This may be in part due to the slow rate at which backward erosion piping advances, as observed in laboratory experiments. Unfortunately, very limited research has been conducted on backward erosion progression rates, making it difficult to assess the timing of development. This study evaluates the progression rate of backward erosion through analyses of small-scale flume experiments conducted on nine uniform sands with median particle diameters ranging from 0.30 to 2.52 mm. Results indicate that pipe progression rate is proportional to seepage velocity, but is also influenced by particle diameter and void ratio of the sand. **DOI: 10.1061/(ASCE)GT.1943-5606.0002338.** © 2020 American Society of Civil Engineers.

Introduction

Backward erosion piping (BEP) refers to a process by which shallow erosion pipes progress upstream through foundation sands beneath water retention structures, as illustrated in Fig. 1. The erosion initiates near the downstream toe when pressures in the foundation sand are sufficient to carry sand particles to the ground surface through either existing defects in the clay layer or heave-induced cracks. After erosion initiates, an erosion channel may form and progress upstream through the foundation sand along the clay cover layer. The channel must follow the cohesive cover layer as it provides a roof over the open erosion channel that forms. If the seepage forces in the foundation sand are sufficient, the pipe will continue to progress upstream. The sand is transported through the erosion channel and carried to the ground surface where it is deposited, often forming a cone of sand commonly referred to as a sand boil. If the erosion pipe can progress to the river or upstream reservoir, uncontrolled erosion can lead to subsidence of the embankment and possible failure. Historically speaking, BEP accounts for approximately one-third of internal erosion-related dam failures ([Richards and Reddy 2007](#)), second only to concentrated leak erosion as the most dangerous form of internal erosion ([Foster et al. 2000](#)). Additionally, recent surveys of levee inventories in the United States have identified BEP as a leading risk factor

for levee failures prior to overtopping ([Baker 2018](#)). Because of its significance, understanding the mechanics of BEP is an issue of importance for engineering practice.

Numerous laboratory investigations have been conducted to investigate the critical conditions that lead to failure from BEP, including de Wit ([1984](#)), Townsend et al. ([1981](#)), van Beek et al. ([2011](#)), and Allan ([2018](#)). These studies have focused on determining the critical average hydraulic gradient, H_{cr}/L, where H_{cr} is the total head loss across the water retention structure, at which BEP completely progresses through the foundation under steady-state conditions (Fig. 1). These studies have led to an understanding of the drivers of BEP progression as summarized by Robbins and van Beek ([2015](#)), as well as predictive methods for determining the critical head, H_{cr}, in practice (e.g., [Sellmeijer and Koenders 1991](#); [Schmertmann 2000](#); [van Beek et al. 2011](#); [Hoffmans and Van Rijn 2018](#)). However, little to no consideration has been given to the time required for BEP to progress through the foundation. For situations with short hydrographs, such as tidal loads and small rivers, the time of development for BEP pipes to form is important in determining the reliability of flood defenses. Even on large rivers such as the Mississippi, field observations have indicated that only a small percentage of BEP initiation cases progress to failure ([DeHaan et al. 2012](#); [Schaefer et al. 2017](#)). While this may be primarily due to the critical head not being reached, it may also be in part due to the limited time for which the critical differential head is exceeded. For these reasons, it is of interest to be able to assess the rate of BEP progression through foundations. This study examines the progression rate of BEP erosion channels through a series of small-scale rectangular flume tests and corresponding finite element simulations. First, this paper reviews available information from the literature regarding BEP progression, and then describes the small-scale flume experiments conducted and analyses of the measured erosion rates.

[1]Civil Engineer, US Army Engineer Research and Development Center, Vicksburg, MS 39180 (corresponding author). ORCID: https://orcid.org/0000-0002-4758-1450. Email: Bryant.A.Robbins@usace.army.mil

[2]Civil Engineer, Geotechnical and Structures Laboratory, US Army Engineer Research and Development Center, 3909 Halls Ferry Rd., Vicksburg, MS 39180.

[3]Professor, Dept. of Civil and Environmental Engineering, Colorado School of Mines, 3909 Halls Ferry Rd., Vicksburg, MS 39180, Golden, CO 80401. ORCID: https://orcid.org/0000-0002-8234-7846

Background

Very little research has been conducted on the rates at which BEP progresses through foundations. The earliest work assessing this

© ASCE   04020093-1   J. Geotech. Geoenviron. Eng.

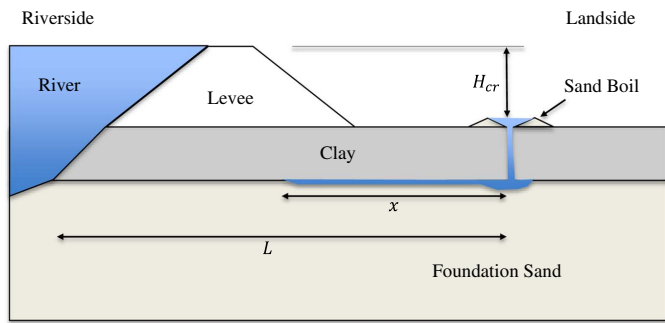J. Geotech. Geoenviron. Eng., 2020, 146(9): 04020093

Fig. 1. Illustration of the process of backward erosion piping.

topic was a theoretical description of the progression rate put forward by Kézdi ([1979](#)), in which the progression rate was considered proportional to the average pore velocity upstream of the pipe. Assuming no head loss occurs in the pipe, the instantaneous pipe progression rate, v_{p-i}, is given by

$$v_{p-i}(t) = \frac{dx}{dt} = \frac{ckH_{cr}}{(L-x)n} \tag{1}$$

where c = constant of proportionality; k = hydraulic conductivity; H_{cr} = critical hydraulic head; L = seepage length; x = pipe length; and n = soil porosity.

Kézdi solved Eq. ([1](#)) and determined the average velocity of the pipe over the length L to be

$$v_p = \frac{2ckH_{cr}}{Ln} \tag{2}$$

Although Kézdi proposed Eqs. ([1](#)) and ([2](#)), it does not appear that the equation was calibrated to laboratory or field data, and no recommendations for the constant of proportionality, c, were made. Sellmeijer et al. ([2011](#)) and Knoeff et al. ([2010](#)) presented a series of full-scale experiments in which the temporal pressure response and mass erosion rates during pipe progression are presented. However, assessment of progression rates from these tests is questionable due to the variable upstream head and intermittent pipe progression that occurred. Van Beek et al. ([2011](#)) conducted experiments in which data regarding the pipe progression rates were collected. However, the progression rates were not presented in the original publication, and no further analysis of the rates was done. Robbins et al. ([2018](#)) presented quantitative measurements of pipe progression rates made in small-scale, cylindrical flume tests that demonstrated that progression rate was indeed proportional to the velocity in the sand upstream of the pipe, as proposed by Kézdi. Allan ([2018](#)) presented further confirmation from large-scale rectangular laboratory tests. Vandenboer et al. ([2019](#)) conducted small-scale flume experiments using upstream heads that substantially exceeded the critical head. By using loads greater than the critical head, the pipe progressed completely through the sample at a fixed hydraulic head such that the influence of average hydraulic gradient on progression rates could be assessed. The results once again confirmed that the pipe progression rate varied linearly with the applied gradient.

Pol et al. ([2019](#)) compiled the information on pipe progression rates from Sellmeijer et al. ([2011](#)), van Beek et al. ([2011](#)), Robbins et al. ([2018](#)), Vandenboer et al. ([2019](#)), and Yao ([2014](#)) to develop two equations for predicting pipe progression rates. The first equation presented by Pol et al. ([2019](#)) was Eq. ([2](#)) as proposed by Kézdi ([1979](#)). By fitting Eq. ([2](#)) to the experimental data set, Pol et al. ([2019](#)) found that $c = 1.6$ best matched the observed progression

rates. The second equation evaluated was derived through a multi-variate regression on the combined data set. The resulting equation is given by

$$\frac{v_p}{\bar{v}_p} = 6.2\left(\frac{H}{L}\right)^{1.4}\left(\frac{k}{\bar{k}}\right)^{0.57} \tag{3}$$

where v_p = pipe progression rate; $\bar{v}_p$ = mean value of v_p for the data set used in the regression; H = differential head across the sample; L = seepage length; k = sample hydraulic conductivity; and $\bar{k}$ = mean value of k for the data set used in the regression.

Although the combined data set consisted of 45 experiments, the data were limited to fine sands with a maximum d_{50} of 0.45 mm. The limited range of sand sizes that were used resulted in the equations being assessed over a very narrow range of seepage velocities, potentially limiting the generality of Eqs. ([2](#)) and ([3](#)). In the present study, uniform sands ranging in median grain size from 0.30 to 2.52 mm were tested. The large range of grain sizes tested (and corresponding seepage velocities) allowed for a thorough evaluation of methods for predicting pipe progression rates.

Experiments

Experimental Apparatus

An acrylic, unidirectional seepage flume was constructed for this laboratory test, as shown in Fig. [2](#). The flume was designed after the small-scale laboratory flume used by van Beek et al. ([2011](#)). The flume was constructed from 25.4-mm-thick (1-in.-thick) acrylic. The internal flume dimensions were $82 \times 30 \times 10$ cm. The entire flume apparatus was fixed to a rotating aluminum frame to facilitate sample preparation and removal. The flume was able to rotate 180°, from a vertical position with the downstream end up for sample preparation to a vertical position with the downstream end down for sample removal. The flume was always fixed in a horizontal position for running the BEP experiments, as illustrated in Fig. [2](#).

The sand sample was confined within the flume by upstream and downstream end walls. The upstream end wall was constructed from 1-cm-thick acrylic perforated with 33 holes, each having a diameter of 1.27 cm. The perforated upstream wall was wrapped in geotextile filter fabric to allow the inflow to diffuse evenly through the plate into the sample. The contact between the inside of the flume and the upstream wall was sealed with a neoprene rubber gasket material and high vacuum grease. The downstream end wall consisted of a 1-cm-thick perforated acrylic plate constructed with a V-shape at the top, with a minimum height of 6.5 cm in the center of the plate and a maximum height of 7.0 cm
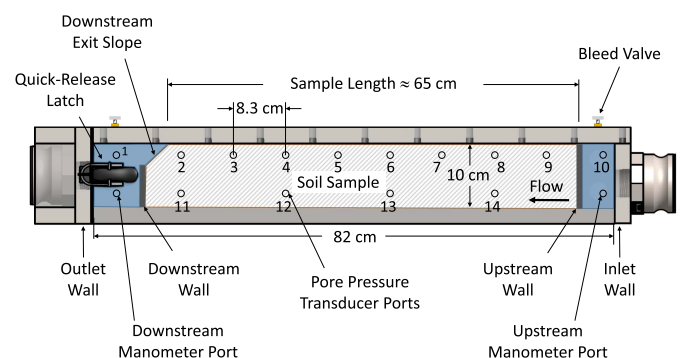

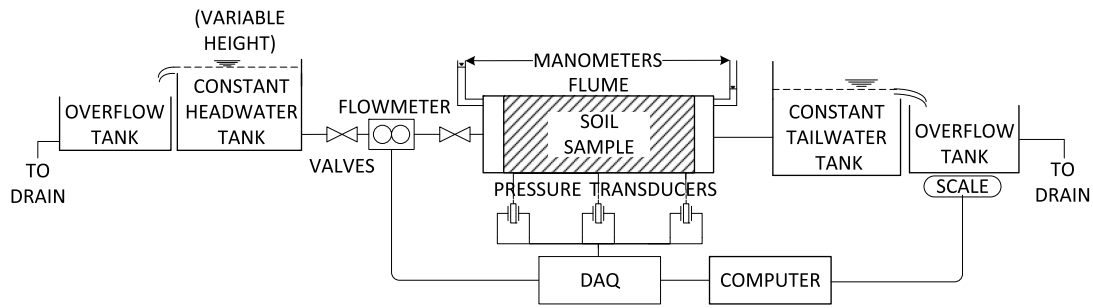**Fig. 2.** Schematic of the small flume apparatus.

Fig. 3. Schematic of experimental setup of small flume device.

on the edges of the plate. Constructing the downstream end wall in a V-shape ensured that the shortest sample length on the top of the sample occurred in the center of the flume for every experiment, such that the BEP process would initiate in the center of the sample as described in Montalvo-Bartolomei et al. (2016). The shortest path through the center of the sample formed when the sand came to equilibrium at its angle of repose after the flume was rotated to the horizontal position. The shortest path was measured from the upstream wall to the top center location of the downstream exit slope of the sample. Previous testing efforts (van Beek et al. 2011; Townsend et al. 1981) ensured that piping occurred in the center of the sample by manually forming the shortest seepage path in the sample center. The addition of the downstream V-shaped end wall eliminated the need for manual formation of the shortest seepage path, leading to more systematic and repeatable testing.

The downstream end wall was supported by spring-loaded supports attached to the removable end cap. The removable end cap, shown in Fig. 2 as the outlet wall, was attached to the flume with two quick release latches such that it could be easily removed for sample preparation and disassembly. The end cap was sealed to the main flume body with a rubber seal and high vacuum grease. As the end cap was secured to the flume body, the spring-loaded supports between the end cap and the downstream end wall gently compressed, ensuring integral contact between the sample and the downstream wall. The flow inlet and outlet consisted of 3.8 cm (1.5-in.) NPT quick connect fittings in the inlet wall and outlet wall as shown in Fig. 2. In addition to the inlet and outlet ports, three bleed valve ports were installed in the top of the flume to assist in saturation of the sample and apparatus. Two of the bleed valves were installed near the downstream end of the flume to aid in removing any air bubbles that may have remained in the apparatus after the end cap was secured. A single bleed valve was installed in the upstream area of the flume to allow all air to be removed from between the upstream sample end wall and the flume inlet wall.

One side wall of the flume was configured with 20 0.25-in. NPT ports for the addition of pore pressure transducers. The position and spacing of the pore pressure ports are shown in Fig. 2. For all experiments, 14 of the pressure transducer ports were connected to Honeywell 26PC (Golden Valley, Minnesota) differential pressure transducers to monitor the seepage-induced pore pressures throughout testing. In addition, two of the ports in the downstream and upstream areas were connected to manual manometers for quick visual verification of measurements. The remaining ports were plugged and unused during testing. A filter fabric was adhered to the inside of the flume over each port to ensure a flush surface at the sample-port interface. The pressure transducers were connected to a National Instruments USB-6218 data acquisition device (National Instruments, Austin, Texas), and the pressures were recorded at 1-s intervals. The data acquisition device was connected to a computer that logged the pressure data to file.

The flume inlet was connected to a constant head tank for all but the coarsest two sands. For the remaining two sands, due to their much larger hydraulic conductivities, the flow rates required to cause BEP exceeded that achievable by the head tank, and the inlet was connected directly to a 1.5-HP pump. A constant head overflow tank was connected to the flume outlet. The flow rate was monitored with an electromagnetic flow meter and verified through manual flow rate measurements made by weighing the outflow captured in 1-min intervals on a scale. A diagram of the complete experimental setup is shown in Fig. 3, and a photograph of the apparatus assembled for testing is provided in Fig. 4.

Materials

A total of nine uniform sands were obtained for flume testing as part of this study. The gradation characteristics obtained in accordance with ASTM D422 (ASTM 2007) for all nine sands are provided in Table 1. Also, the minimum ($\gamma_{d,\min}$) and maximum ($\gamma_{d,\max}$) dry unit weights were obtained for each sand according to the procedures in ASTM D4254 and D4253 (ASTM 2016a, b), respectively. The mason sand was procured from a local quarry in Vicksburg, MS. The remaining eight sands were obtained from a quarry in Brady, Texas. Because these sands were obtained from the same source, they had similar roundness and specific gravity. According to the manufacturer's specifications, the specific gravity was 2.65. Particle roundness has been shown to have a minor
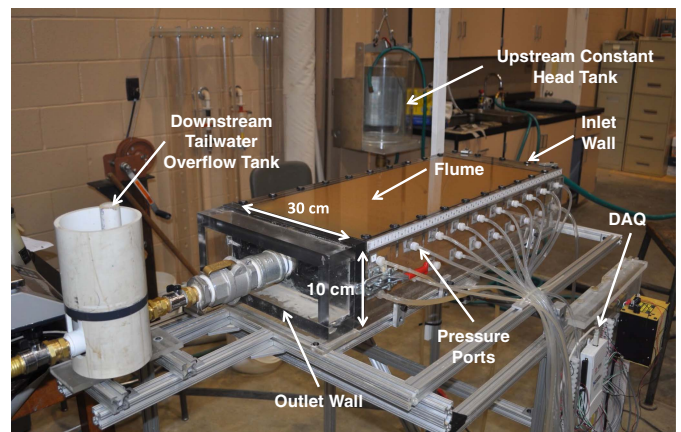

Fig. 4. Photograph of assembled flume apparatus ready for testing. (Image by A. M. Montalvo-Bartolomei.)

© ASCE 04020093-3 J. Geotech. Geoenviron. Eng.

J. Geotech. Geoenviron. Eng., 2020, 146(9): 04020093

Table 1. Sand gradation characteristics

Sand type	d_{10} (mm)	d_{15} (mm)	d_{50} (mm)	d_{60} (mm)	d_{70} (mm)	C_u	C_c	$\gamma_{d,\min}$ (kN/m³)	$\gamma_{d,\max}$ (kN/m³)
Mason sand	0.22	0.24	0.33	0.36	0.39	1.61	1.00	14.66	17.17
40–70	0.23	0.24	0.30	0.32	0.35	1.42	0.98	14.42	16.69
30–50	0.32	0.34	0.43	0.45	0.49	1.42	0.98	14.61	16.96
20–40	0.47	0.49	0.61	0.64	0.69	1.39	0.98	14.80	17.11
16–30	0.64	0.67	0.85	0.91	0.95	1.41	0.98	14.91	17.14
12–20	0.89	0.93	1.13	1.20	1.30	1.34	0.96	14.70	16.82
8–16	1.27	1.31	1.57	1.65	1.70	1.30	0.97	14.95	17.19
8–12	1.59	1.71	2.29	2.44	2.60	1.54	1.02	15.00	16.90
6–9	2.02	2.09	2.52	2.64	2.80	1.31	0.97	14.95	16.81
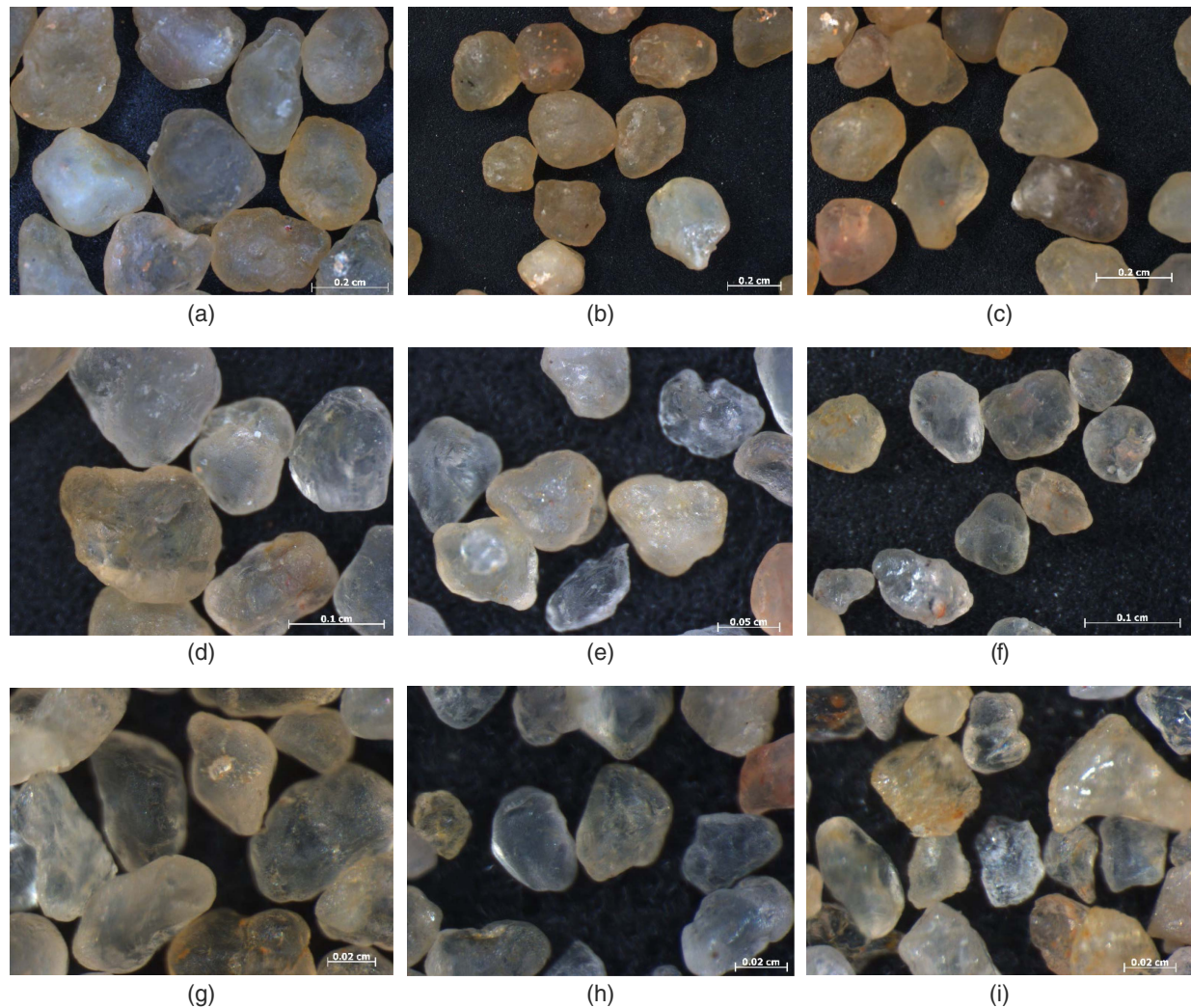
Fig. 5. Microscope images of sands: (a) 6–9; (b) 8–12; (c) 8–16; (d) 12–20; (e) 16–30; (f) 20–40; (g) 30–50; (h) 40–70; and (i) mason sand. (Images by Erin R. Reed-Gore.)

influence on critical heads for pipe progression (Sellmeijer et al. 2011), and thus it can also influence the velocity of pipe progression. The particle roundness was therefore quantified through image analysis using the software ImageJ version 1.46r (Ferreira and Rasband 2012). Microscope images of the sands (Fig. 5) were thresholded in ImageJ to identify the individual particles, and the roundness was subsequently computed. The resulting roundness varied from 0.63 to 0.83 with a mean value of 0.76.

Sample Preparation Procedure

The flume apparatus was rotated to the vertical position, and the downstream end cap (outlet wall) was removed so that the inside of the flume was accessible for sample placement. The upstream water supply hose was entirely saturated and connected to either the constant head tank or recirculating pump, depending on the hydraulic conductivity of the sand being tested. For all experiments, the following sample preparation procedures were followed:

© ASCE   04020093-4   J. Geotech. Geoenviron. Eng.

J. Geotech. Geoenviron. Eng., 2020, 146(9): 04020093

1. The water level in the flume was increased until the flume was approximately half filled prior to placing any sand in the flume. All submerged flume components were checked to ensure that no air was present. Measures were taken to remove any air that was observed. Ensuring saturation of the system prior to sand placement was the only way to ensure that air would not interfere with the experiment.

2. Oven-dried sand was then slowly rained (pluviated) into the water in the flume from a hand scoop or hopper. For dense samples, the sand was rained into the flume in 10-cm layers. Each layer was compacted through repeated insertion of a 2.54 cm (1-in.)-diameter steel rod prior to placing the next layer. The sand was compacted until no further densification was observed. In this manner, each dense layer was compacted to the maximum density obtainable by the method in order to obtain a uniformly dense sample. For loose samples, the sand was continuously placed while avoiding vibrations until the entire sample volume was filled.

3. As the sand was being placed, the water level in the flume device would gradually rise. As each set of pore pressure transducer lines became submerged, care was taken to ensure that all air was flushed from the lines. The air was purged from each additional set of transducers prior to sand reaching the transducer locations, which ensured that air would not become trapped in the sample.

4. After the sand was placed, the downstream V-shaped terminal wall with the springs was placed directly on the sample. The downstream end cap was secured to the flume with the latches. Water was manually added through the downstream outflow valve until all air was removed from the fittings and flume. The downstream overflow tank was attached to the flume and saturated. The final weight and volume of the sample were obtained to calculate the density of the sample. All required hoses were attached, and the flume was rotated to the horizontal position for testing. The shortest seepage length was measured from the upstream end wall to the top of the downstream exit slope.

Test Procedure

The following steps were taken to run each laboratory BEP test:

1. Prior to initiating flow, data acquisition was initiated, and all pore pressure transducers were zeroed to the downstream tailwater level to ensure a consistent datum for pressure measurements.

2. For tests using the constant head tank, the head tank was set to an elevation slightly above the tailwater elevation. For tests using the recirculating pump, the pump was turned on with all the flow passing through the recirculation line. All valves attached to the flume were opened so that the flow was controlled either by raising the head tank or opening the control valve on the inflow line attached to the pump.

3. The flow was gradually increased until a low initial value (typically 0.05) of the average hydraulic gradient was obtained across the sample. The sample sat in equilibrium at this initial value for some time while measures were taken to ensure that all instrumentation (pressure, flow, and video) were responding and recording correctly.

4. The flow was gradually increased in intervals corresponding to changes in gradient of 0.02–0.05. At each flow increment, the sample sat for a minimum of 5 min. If no visible particle movement was observed, the flow was increased further.

5. After any particle movement was visually observed near the downstream slope of the sample, the flow increments were reduced to an amount corresponding to a change in average hydraulic gradient of 0.01 until active BEP was observed. Although some particles moved prior to active pipe progression, the movement was limited to small numbers of particles (1–6) displacing at the downstream exit slope with periods of equilibrium in between particle movement observations. Because only a few particles moved, the sample length was relatively unchanged. Therefore, these minor movements had no impact on the measured value of the critical differential head and corresponding pipe progression rates. When the critical differential head was reached, an active pipe channel would form due to a group of grains near the exit eroding all at once, and all pressure readings dropped as the piping process progressed. This pipe channel would then continuously progress through the sample without reaching equilibrium at any point. This behavior was anticipated, according to the work of van Beek et al. (2014), in which small-scale experiments with large seepage exit areas are controlled by initiation conditions. The position of the pipe tip was marked with time on the acrylic as it progressed upstream. The test was completed once the pipe reached the upstream wall. The inlet valve was closed, and final observations were noted.
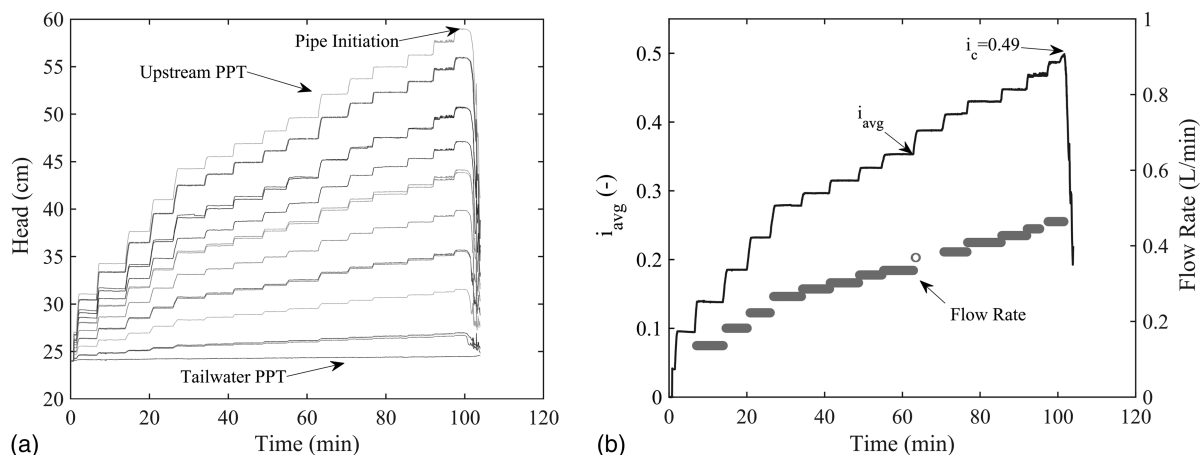

Fig. 6. Example: (a) pore pressure measurements; and (b) corresponding average hydraulic gradient and flow rate measurements for Test 4 on 40–70 sand.
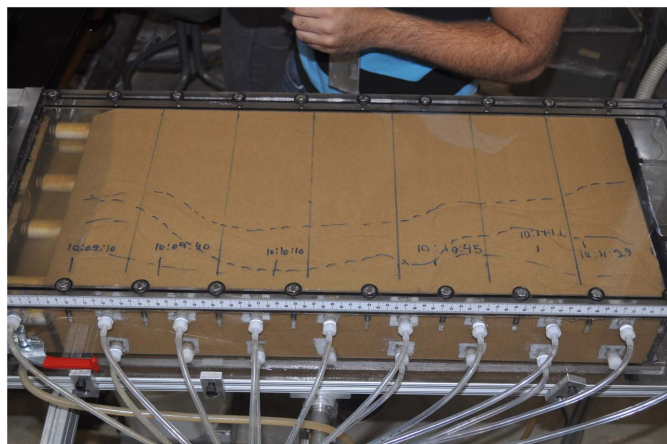
© ASCE   04020093-5   J. Geotech. Geoenviron. Eng.

J. Geotech. Geoenviron. Eng., 2020, 146(9): 04020093

Fig. 7. Final pipe path for Test 4 on 40–70 sand. (Image by Jamie F. Lopez-Soto.)
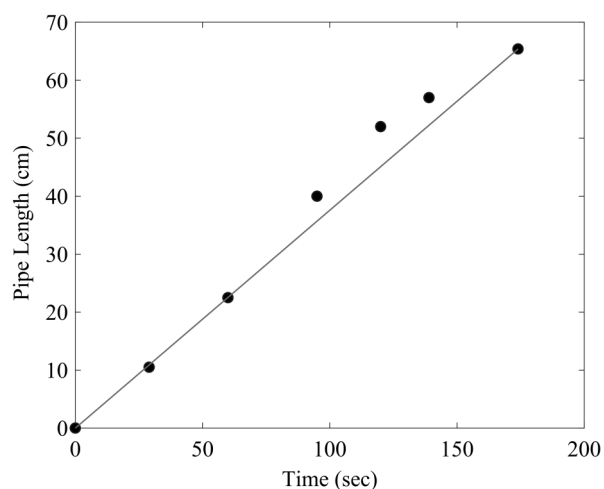

Fig. 8. Pipe position as a function of time and corresponding average progression rate for Test 4 on 40–70 sand.

Test Results

Typical data obtained from a single test are shown in Figs. 6–8. The average hydraulic gradient across the sample, i_{avg}, was calculated as the slope of a least-squares linear fit of the pore pressure transducers in the sample relative to their locations. For all experiments, the coefficient of determination of this fit was greater than 0.99, indicating highly linear headloss, which suggests the samples are quite uniform. The time history of i_{avg} for the pore pressure record shown in Fig. 6(a) is provided in Fig. 6(b) along with the associated flow rate. From the pore pressure record in Fig. 6(a) and the i_{avg} record in Fig. 6(b), it is readily seen by the stepwise constant values that the sample is stable until the moment of erosion initiation. After erosion initiates, the pore pressures and average gradient rapidly fall as the pipe progresses through the sample. Fig. 7 provides a photograph of the final pipe path for this particular test. For tests where the pipe progressed relatively slowly, the pipe position was noted through time by marking the flume, as shown in Fig. 7. For the smallest sands, the pipe often split into two or more pipes as the meandering pipe progressed. Only the positions of the furthest pipe tip from the downstream slope were marked. For tests where the pipe progressed quickly through the sample, the pipe position as a function of time was extracted from the video records of the test. In both cases, a time record of the pipe position was obtained. The average progression rate was calculated as the slope of a line connecting the first and last point in the time record (Fig. 8). For all tests, the measured values of sample dry unit weight (γ_d), void ratio (e), sample length (L), exit slope angle (θ), critical value of i_{avg} at erosion initiation (i_c), hydraulic conductivity prior to erosion (k), and average value of the pipe progression rate (v_p) are reported in Tables 2 and 3. The following sections present an assessment of the pipe progression rates.

Analyses of Progression Rates

The average pipe progression rate has been proposed to be proportional to the seepage velocity, as described by Eqs. (2) and (3). The performance of these equations is first assessed on the basis of average, horizontal, hydraulic gradients across the sample. The local, horizontal, hydraulic gradient, i_{local}, near the pipe tip is then

Table 2. Test results for mason sand

Sand type	Test number	i_c	γ_d (kN/m³)	e	k (m/s)	L (m)	θ	v_p (cm/s)
Mason sand	4-1	0.55	16.98	0.53	3.82×10^{-4}	0.664	39.2	—
	5-1	0.39	16.99	0.53	4.16×10^{-4}	0.653	39.8	0.19
	7-1	0.56	17.12	0.52	3.50×10^{-4}	0.662	39.2	0.55
	8-1	0.33	16.19	0.60	6.67×10^{-4}	0.655	35.0	0.11
	9-1	0.29	15.38	0.69	8.45×10^{-4}	0.650	29.7	0.08
	10-1	0.26	15.55	0.67	7.99×10^{-4}	0.657	36.3	0.07
	12-1	0.27	15.54	0.67	8.79×10^{-4}	0.642	32.0	0.11
	13-1	0.30	15.35	0.69	8.68×10^{-4}	0.642	33.4	0.23
	17	0.25	15.28	0.70	8.67×10^{-4}	0.642	32.9	0.12
	18	0.24	15.37	0.69	8.60×10^{-4}	0.643	34.0	0.08
	19	0.23	15.50	0.68	8.21×10^{-4}	0.645	35.5	0.06
	23	0.26	15.43	0.68	8.16×10^{-4}	0.646	35.5	0.10
	25	0.23	15.35	0.69	8.75×10^{-4}	0.651	38.5	0.16
	28	0.31	15.57	0.67	7.67×10^{-4}	0.645	35.0	0.14
	29	0.44	16.95	0.53	4.17×10^{-4}	0.656	36.7	0.25
	30	0.42	17.04	0.52	4.23×10^{-4}	0.656	39.8	0.17
	31	0.48	17.03	0.53	3.80×10^{-4}	0.655	38.5	0.42
	32	0.40	17.06	0.52	4.15×10^{-4}	0.653	39.1	0.11
	33	0.36	17.12	0.52	4.00×10^{-4}	0.652	39.1	0.15
	34	0.40	17.12	0.52	3.67×10^{-4}	0.656	41.9	0.22

© ASCE 04020093-6 J. Geotech. Geoenviron. Eng.

J. Geotech. Geoenviron. Eng., 2020, 146(9): 04020093

Table 3. Test results for uniform sieved sands

Sand type	Test number	i_c	γ_d (kN/m³)	e	k (m/s)	L (m)	θ	v_p (cm/s)
40–70	1	0.23	14.59	0.78	1.15×10^{-3}	0.645	36.7	0.11
	2	0.22	14.67	0.77	1.22×10^{-3}	0.645	41.2	0.15
	3	0.52	16.65	0.56	5.13×10^{-4}	0.649	38.5	0.51
	4	0.49	16.43	0.58	5.26×10^{-4}	0.654	39.8	0.38
30–50	1	0.23	14.92	0.74	2.32×10^{-3}	0.650	40.1	0.21
	2	0.27	14.88	0.75	2.20×10^{-3}	0.647	38.5	0.27
	3	0.50	16.59	0.57	1.03×10^{-3}	0.656	39.1	0.47
	4	0.52	16.57	0.57	1.00×10^{-3}	0.657	40.5	0.41
20–40	1	0.30	15.23	0.71	4.51×10^{-3}	0.646	37.6	0.43
	2	0.27	15.19	0.71	4.19×10^{-3}	0.650	39.8	0.40
	3	0.30	15.13	0.72	4.48×10^{-3}	0.653	40.5	0.54
	5	0.59	16.67	0.56	2.11×10^{-3}	0.656	38.5	1.07
	6	0.58	16.65	0.56	2.15×10^{-3}	0.663	41.9	1.30
16–30	1	0.34	15.26	0.70	6.14×10^{-3}	0.652	41.2	0.62
	2	0.29	15.15	0.71	6.90×10^{-3}	0.649	38.5	0.53
	3	0.53	16.70	0.56	3.36×10^{-3}	0.658	39.8	1.65
	4	0.59	16.66	0.56	3.13×10^{-3}	0.660	36.7	1.16
12–20	1	0.32	15.21	0.71	1.11×10^{-2}	0.649	41.2	0.84
	2	0.30	14.99	0.73	1.28×10^{-2}	0.649	41.2	1.07
	3	0.52	16.49	0.57	5.57×10^{-3}	0.660	40.5	1.61
	4	0.54	16.53	0.57	5.93×10^{-3}	0.662	44.2	1.16
8–16	2	0.66	16.62	0.56	1.34×10^{-2}	0.664	44.1	3.91
	3	0.30	15.11	0.72	2.77×10^{-2}	0.664	52.4	1.79
	5	0.31	15.13	0.72	2.60×10^{-2}	0.658	41.2	1.03
	6	0.65	16.73	0.55	1.31×10^{-2}	0.662	44.2	4.41
	7	0.72	16.51	0.57	1.32×10^{-2}	0.668	44.2	5.00
8–12	4	0.53	16.57	0.57	2.21×10^{-2}	0.660	42.6	2.00
	5	0.58	16.64	0.56	2.03×10^{-2}	0.658	41.2	1.99
	6	0.35	15.11	0.72	3.57×10^{-2}	0.660	47.6	1.05
	7	0.32	15.05	0.73	3.87×10^{-2}	0.659	47.6	1.35
6–9	4	0.36	15.02	0.73	3.99×10^{-2}	0.658	44.2	1.57
	5	0.62	16.45	0.58	2.30×10^{-2}	0.662	45.0	4.73
	7	0.63	16.42	0.58	2.31×10^{-2}	0.662	44.2	3.15
	9	0.66	16.56	0.57	2.18×10^{-2}	0.668	54.5	4.18
	10	0.32	14.96	0.74	4.05×10^{-2}	0.657	43.4	—
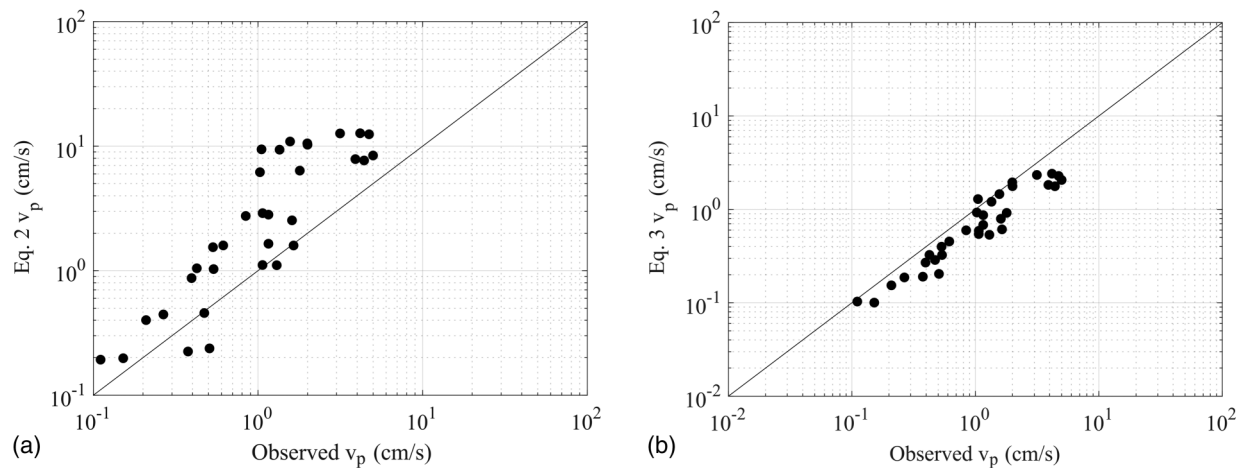
Fig. 9. Pipe progression rate predictions from (a) Eq. (2); and (b) Eq. (3).

estimated using numerical models of the pipe progression to determine if a better estimate of the pipe advancement rate can be obtained from the local seepage velocity.

Pipe Rates from Average Gradients

The performances of Eqs. (2) and (3) were evaluated by calculating the pipe progression rates for all experiments. When applying Eq. (2), the best fit value of $c = 1.6$, as suggested by Pol et al. (2019), was used in the predictions. The hydraulic conductivity, porosity, and average hydraulic gradient were obtained from Tables 2 and 3. When applying Eq. (3), the values of $\bar{v}_p$ and $\bar{k}$ were 6.5×10^{-4} and 3.4×10^{-4} m/s, respectively, based on the calibration data set used by Pol et al. (2019). The predicted pipe progression rates were compared to the observed pipe progression rates in Fig. 9(a) for Eq. (2) and Fig. 9(b) for Eq. (3), respectively.
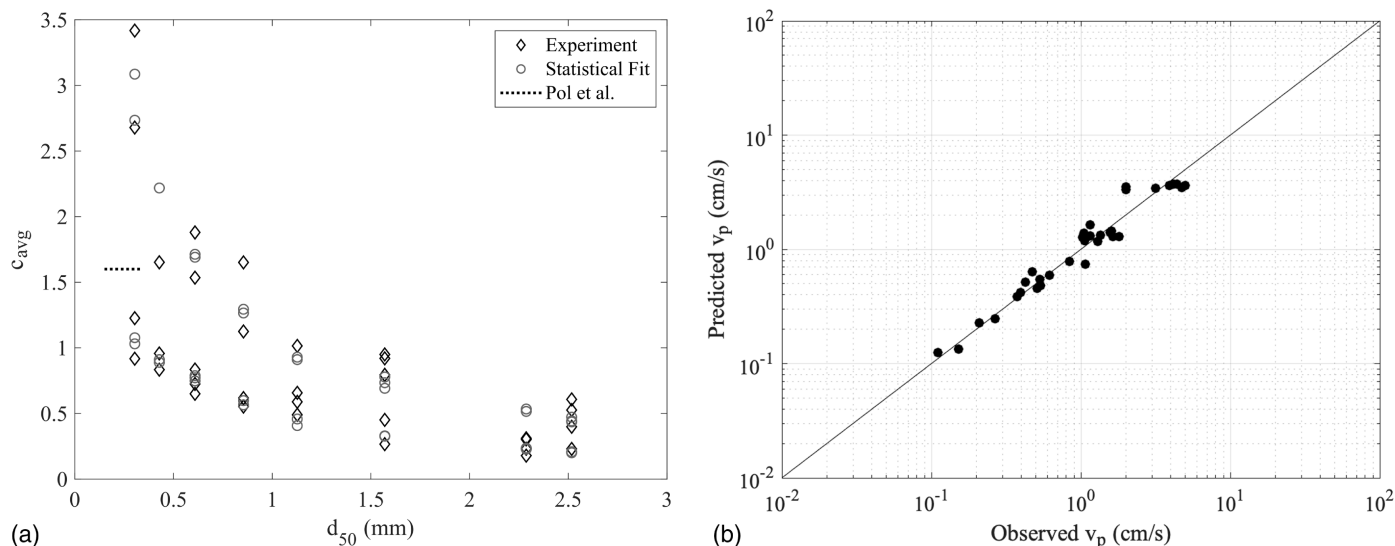
© ASCE   04020093-7   J. Geotech. Geoenviron. Eng.

J. Geotech. Geoenviron. Eng., 2020, 146(9): 04020093

Fig. 10. Eq. (1): (a) back-calculated c values for all tests, statistically predicted c value using Eq. (3), and constant c value from Pol et al. (2019); and (b) predicted pipe progression rates using c values from Eq. (3).

From Fig. 9, it is readily seen that Eq. (2) overpredicts the progression rate, while Eq. (3) underpredicts the progression rate.

To improve the predictions of average pipe progression rate based upon the average hydraulic gradient, the coefficient c in Eqs. (1) and (2) was back-calculated for all of the experiments in Table 3. The back-calculated, or experimental, values are plotted in Fig. 10(a), from which it is immediately evident that c varies with grain size. Further, because only void ratio varies for each test series at a given grain size, c must also vary with void ratio as indicated by the range of calculated values for c for each sand. To capture the trends observed in the back-calculated c values, a statistical fit of the experimental data was conducted, resulting in the following equation for c:

$$c_{avg} = 0.556 \left(\frac{d_{50}}{\bar{d}_{50}}\right)^{-0.87} \left(\frac{e}{\bar{e}}\right)^{-3.30} \tag{4}$$

where c_{avg} = best fit value of c based on *average* gradients; d_{50} = median grain size; $\bar{d}_{50}$ = mean value of the median grain size for all tests; e = void ratio of the sample; and $\bar{e}$ = mean value of the void ratio for all tests.

The regression yielded a coefficient of determination of 0.93 with p-values on the order of 10^{-12} or less for all three regression coefficients. The predicted values of c obtained using Eq. (4) are plotted in Fig. 10(a). The constant value of $c = 1.6$ used by Pol et al. (2019) is also shown. Interestingly, the value of c used by Pol et al. (2019) aligns nicely with the median trend of the back-calculated c values in the range of associated grain sizes. Further, it is readily seen that Eq. (4) captures the general trends observed in c due to both grain size and void ratio. Using Eqs. (4) and (2) together leads to improved predictions of pipe progression rate [Fig. 10(b)].

Pipe Rates from Local Gradients

While determining c as a function of grain size and void ratio improved the predictions of pipe progression rate based on average gradient, the magnitude of c based on average gradients was larger than 1 for the finer sands. This suggests that the pipe is progressing faster than the average seepage velocity. In reality, concentrated flow near the upstream end of the pipe results in local velocities much higher than the average seepage velocity. To estimate the physical value of c relative to the local seepage velocities driving pipe progression, an attempt was made to evaluate c using estimates of local hydraulic gradients near the pipe tip. To analyze pipe progression on the basis of local gradients, it was necessary to numerically model pipe progression. As will be demonstrated from the modeling, the pore pressure transducers did not provide reliable estimates of local gradient because they were located on the outer boundary of the domain.

A 3D finite element (FE) model specifically formulated for modeling BEP (Fig. 11) was used to simulate the tests (Robbins and Griffiths 2018). The model simulates BEP progression in a piecewise, steady-state manner using soil elements and pipe elements. The flow in the soil elements is treated as steady-state groundwater flow governed by the Laplace equation for isotropic soils. The flow in the pipe elements is treated as laminar flow through wide, shallow rectangular pipe channels. The assumption of laminar flow has been shown to be reasonable for $d_{50} < 1$ mm (van Beek et al. 2019), but may not be valid for the three coarse sands in this study. Nevertheless, laminar flow was assumed for all sands due to the limitations of the available model. The depth of the
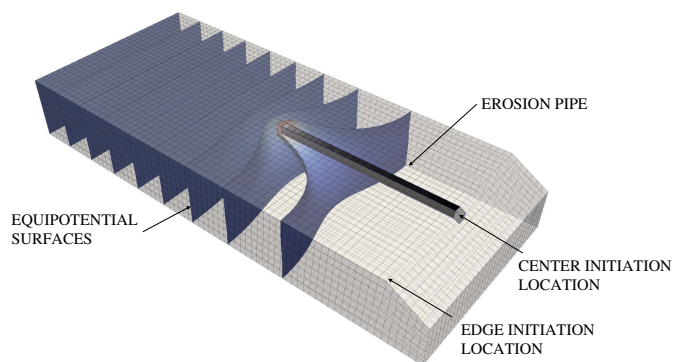

Fig. 11. Illustration of 3D finite element model used to evaluate the local hydraulic gradient near the pipe tip.

pipe is determined based on the critical hydraulic shear stress of the sand and the flow conditions in the pipe. The hydraulic conductivity of the pipe elements is then determined based on the resulting dimensions of the pipe channel. For complete model details, the interested reader is referred to Robbins and Griffiths (2018).

A separate analysis was conducted for each experiment listed in Table 3. Given that the geometry of each sample was nearly identical for all tests, the same base mesh was used. The mesh consisted of 1-cm hexahedral elements, as shown in Fig. 11. For each analysis, the downstream boundary (slope and vertical face) was set to a constant head boundary condition of 0.0. The upstream boundary condition was then set to a constant head corresponding to the i_c value listed for each test in Table 3. The hydraulic conductivity for each analysis was set to the measured value in Table 3. The critical shear stress of the sand used in computing the pipe hydraulics was obtained from the simple relationship $\tau_c(Pa) = d_{50}$ (mm) as suggested by Briaud et al. (2017). In the laboratory tests, the pipe would meander along the top surface of the flume. As a result, in some experiments the pipe meandered toward the wall with pressure measurements, and in some experiments it meandered away from the wall with pressure measurements. To bracket the range of expected sensor responses, FE analyses were conducted in which the pipe was initiated at the downstream edge adjacent to the wall of the flume (Fig. 11). This was done to examine the simulated pore pressure transducer response expected if the pipe were to pass along either wall of the flume (adjacent to the sensors or opposite the sensors). The modeled response is compared with the measured response in Fig. 12 for Test 2 on 30–50 sand for which the pipe pattern is shown in Fig. 13. Toward the downstream end of the sample, the pipe travelled away from the sensors. As such, the measured pressures are similar to the FE prediction assuming the pipe is opposite the sensor wall (FE, Far). At a location of $x = 30$ cm, the pipe began to meander back toward the sensor wall. As such, the measured pressure response began moving toward the FE prediction assuming the pipe is near the sensor wall (FE, Near). Because of this dependency on pipe position, calculation of local gradients upstream of the pipe using the sensor data led to highly variable results. Instead, an attempt was made to estimate the local gradient directly from the numerical model.

To estimate the local gradient upstream of the pipe, the pipe was initiated in the center element on the top of the slope and was allowed to propagate through the mesh as shown in Fig. 11. The value of the local, horizontal, hydraulic gradient in the element
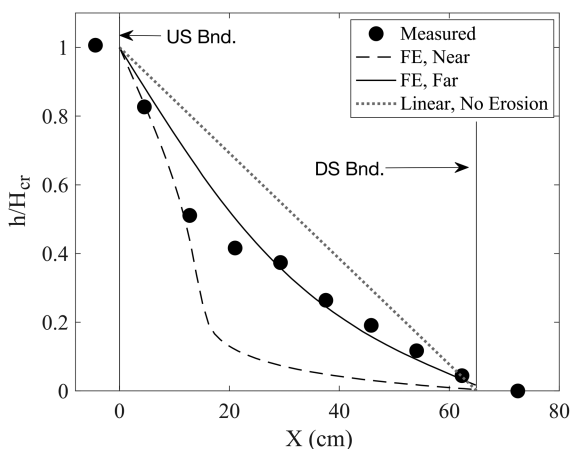

Fig. 13. Pipe pattern in Test 2 on 30–50 sand. (Image by Jamie F. Lopez-Soto.)

upstream of the pipe tip (i_{local}) was recorded at each pipe progression step. While differences in the pipe hydraulics resulted in minor differences in the local gradient values, the value of i_{local} normalized to the average hydraulic gradient across the sample, i_{avg}, was practically identical at each pipe position for all tests assessed (Fig. 14).

Using the values of i_{local} calculated from the FE model, Eq. (1) should be calibrated for use with the local values of i_{local} instead of Eq. (2) because the actual seepage velocity near the pipe tip is being estimated rather than the average hydraulic gradient across the sample. The calibration is performed by back-calculating the appropriate values of c_{local}, that is, the value of c for use with local hydraulic gradients. The best fit value of c_{local} for each test was calculated by first calculating the average pipe progression rate for the FE calculations using i_{local} in Eq. (1) with $c = 1$ as

$$v_{p-fem} = \frac{\sum d_i}{\sum t_i} = \frac{\sum d_i}{\sum d_i/v_{p,i}} = \frac{\sum d_i}{\sum d_i/\left(\frac{ki_{local,i}}{n}\right)} \quad (5)$$

where d_i = distance the pipe travels in each analysis increment; and $t_i = d_i/v_{p,i}$ = time it would take the pipe to travel over that interval

Fig. 12. Comparison of head profiles from finite element model with pipe along sensor wall (Near) and opposite sensor wall (Far) to measured response for Test 2 on 30–50 sand with the pipe at X = 15 cm.
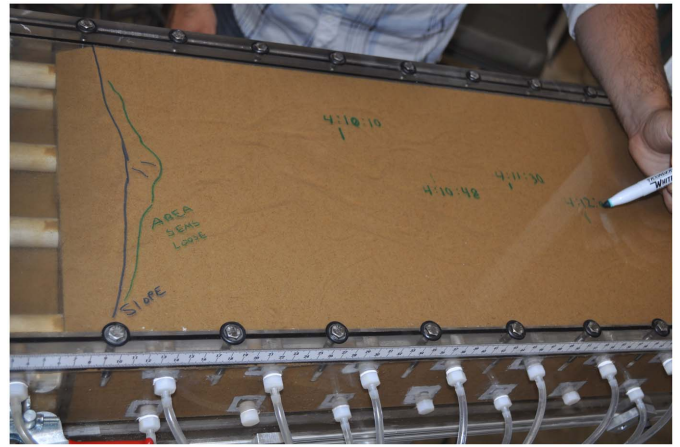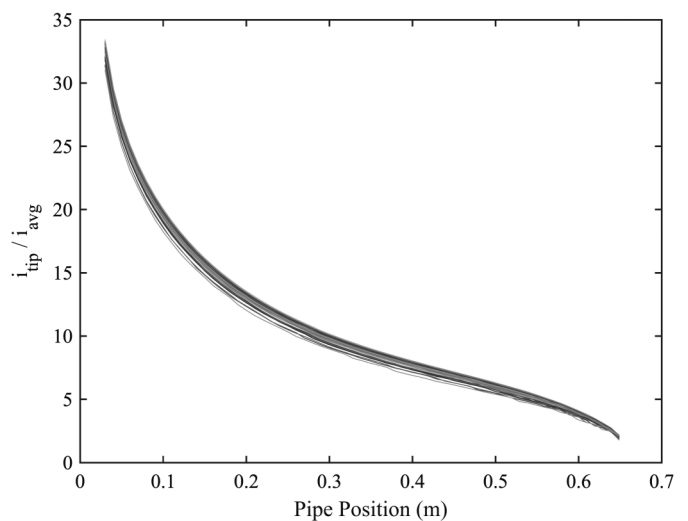

Fig. 14. Normalized, horizontal hydraulic gradient over 1 cm in front of the pipe as a function of pipe position for all tests.
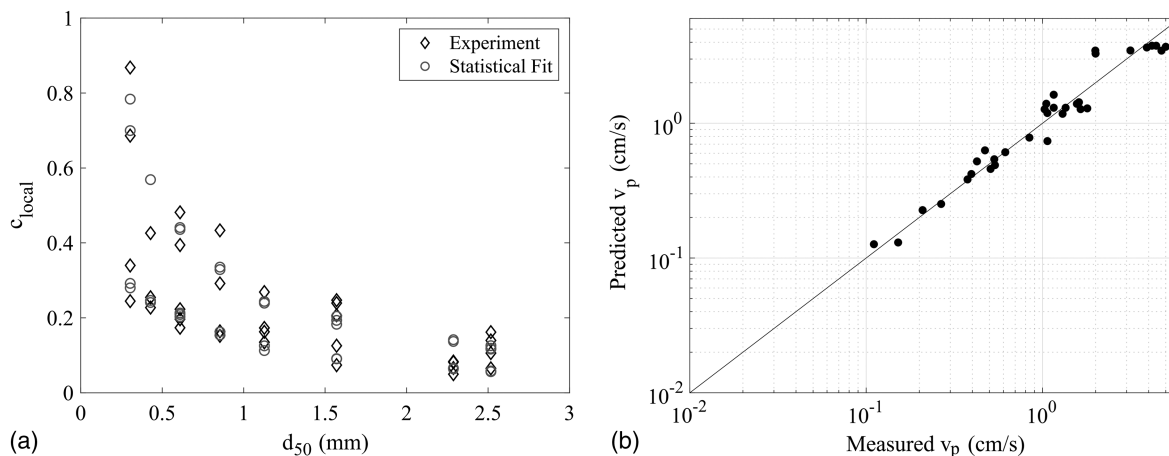
Fig. 15. (a) Back-calculated values of c using local gradient values and corresponding Eq. (4) fit; and (b) predicted pipe progression rates obtained using local gradient estimates with Eqs. (4) and (1).

if traveling at a pipe progression rate of $v_{p,i} = (ki_{local,i})/n$. The best fit value of c_{local} is then calculated as

$$c_{local} = \frac{v_{p-fem}}{v_{p-obs.}} \tag{6}$$

The value of c_{local} was calculated in this manner for each test. The back-calculated values are shown in Fig. 15(a). Because of the consistency of i_{local}/i_{avg} exhibited in Fig. 14 for all tests, the analysis of local gradients simply results in c_{local} values that are a scaled version of the c_{avg} values given in Fig. 10. As such, the trends in Fig. 15(a) are indentical to those in Fig. 10(a). A statistical fit of the back-calculated c_{local} values yielded the following predictive equation:

$$c_{local} = 0.15\left(\frac{d_{50}}{d_{50}}\right)^{-0.84}\left(\frac{e}{e}\right)^{-3.10} \tag{7}$$

where the dependent variables are the same as described for Eq. (4). The coefficient of determination was again 0.93, and the p-values for all regression coefficients were 10^{-12} or less. The average pipe progression rates were then estimated for all tests using the local hydraulic gradients from the FE calculations to estimate local pipe progression rates at each progression step using Eqs. (1) and (7). As shown in Fig. 15(b), this approach yields the same results as the average gradient calculations for this experiment series.

Discussion

Eq. (2) was suggested by Kézdi (1979) as a means of predicting pipe progression rates based on average hydraulic gradients upstream of the erosion pipe. Pol et al. (2019) calibrated Eq. (2) based on a series of 45 laboratory piping experiments and put forward Eq. (3) as an alternate predictive equation, once again on the basis of average hydraulic gradients in laboratory experiments. In this work, the ability of both equations to predict pipe progression rates was assessed by comparing the predicted pipe progression rates to progression rates measured in a series of small-scale laboratory piping experiments. Both equations were found to provide only order of magnitude estimates of the pipe progression rates. Eq. (2) systematically overestimated pipe progression rates by as much as a factor of 10, while Eq. (3) systematically underestimated pipe progression rates by up to a factor of 3. Because overestimating

pipe progression rates will lead to a conservative assessment, Eq. (2) is preferred for preliminary assessments.

To attempt to improve the predictions, an assessment of the experimental values of the c coefficient in Eqs. (1) and (2) was performed on the basis of both average hydraulic gradient and estimated local hydraulic gradient near the pipe tip. Kézdi's approach was selected for use in further analyses due to its physical basis. The assessment of the experimentally determined values of c demonstrated that the pipe progression rate is not only a function of the seepage velocity near the pipe tip, but is also influenced by the median grain size and void ratio of the sand. The influence of void ratio on pipe progression rates was previously identified by Robbins et al. (2018), but the significance of grain size on pipe progression rates has not been previously identified. Further studies will explore mechanics-based explanations for this dependency.

While values of c were determined on the basis of both local (c_{local}) and average (c_{avg}) gradients, the two calculated values were proportional to one another due to the constant proportionality between i_{avg} and i_{local} observed in the FE modeling results (Fig. 12). Values of c_{avg} were high, often greater than 1.0, indicating that the pipe progresses faster than the average seepage velocity through the domain—this is due to the highly concentrated flow near the pipe tip that results in high local seepage velocities near the pipe. Given that the locally calculated gradients are much higher than the average gradients, the values of c_{local} are much lower, indicating that the pipe actually progresses at velocities lower than the pore seepage velocity immediately upstream of the pipe. Improved predictions were obtained by using either c_{avg} as predicted by Eq. (4) with average gradients or c_{local} as predicted by Eq. (7) with local gradients estimated from FE models. However, predicting pipe progression rates on the basis of local hydraulic gradients is thought to represent a more accurate approach for general geometries and boundary conditions. Further research with different boundary value problems is needed to test these concepts in a more general sense.

Conclusions

The progression rate of backward erosion pipes in uniformly graded sands was assessed through a series of small-scale laboratory flume experiments. Equations previously proposed by Kézdi (1979) and Pol et al. (2019) for predicting pipe progression rates on the basis of average hydraulic gradients were found to provide

rough estimates of the progression rates. Analyses of the experimentally observed progression rates revealed that the pipe advancement rate is not only a function of the seepage velocity, but also of grain size and void ratio in uniform sands. Modification of the Kézdi equation to incorporate the influence of grain size and void ratio led to improved predictions of pipe progression rates for analyses, whether based on average hydraulic gradients or local hydraulic gradients near the pipe tip, for the experiments presented, due to the constant proportionality between i_{avg} and i_{local}. For general cases of arbitrary geometry and boundary conditions, assessing pipe progression rates on the basis of local seepage velocities may prove to be the more accurate approach; however, further research is needed to evaluate the validity of the concepts presented for general problem geometries over a range of problem scales.

Data Availability Statement

All data, models, or code generated or used during the study are available from the corresponding author by request.

Notation

The following symbols are used in this paper:

c = constant of proportionality between pore velocity and pipe progression rate;

c_{avg} = value of c based on average hydraulic gradient;

c_{local} = value of c based on local hydraulic gradient;

C_u = coefficient of uniformity $(-)$;

C_u = coefficient of curvature;

d_{50} = median grain size (m);

$\bar{d}_{50}$ = mean value of median grain size in present study (m);

e = soil void ratio;

$\bar{e}$ = mean value of void ratio for all flume tests in the present study (m);

H = differential head across a structure (m);

H_{cr} = critical value of differential head for pipe progression (m);

i_{avg} = average hydraulic gradient across the sample;

i_c = critical value of i_{avg} causing initiation of backward erosion piping;

i_{local} = local hydraulic gradient near the pipe tip;

k = hydraulic conductivity (m/s);

$\bar{k}$ = mean value of k for the calibration data set in Pol et al. (2019) (m/s);

L = seepage length (m);

n = soil porosity;

v_p = pipe progression rate (m/s);

v_{p-i} = instantaneous pipe progression rate (m/s);

$\overline{v_p}$ = mean value of v_p for the calibration data set in Pol et al. (2019) (m/s);

γ_d = dry unit weight of the soil (kN/m^3);

τ_c = critical boundary shear stress for incipient motion of sand (Pa); and

θ = inclination angle of the exit slope relative to horizontal (degrees).

References

Allan, R. 2018. "Backward erosion piping." Ph.D. dissertation, School of Civil and Environmental Engineering, Univ. of New South Wales.

ASTM. 2007. *Standard test method for particle-size analysis of soils (withdrawn 2016)*. ASTM D422-63(2007)e2. West Conshohocken, PA: ASTM.

ASTM. 2016a. *Standard test methods for minimum index density and unit weight of soils and calculation of relative density*. ASTM D4254-16. West Conshohocken, PA: ASTM.

ASTM. 2016b. *Standard test methods for maximum index density and unit weight of soils using a vibratory table*. ASTM D4253-16e1. West Conshohocken, PA: ASTM.

Baker, C. 2018. "USACE conducts first analysis of risk and benefits of USACE levees." In Vol. 11 of *Flood risk management newsletter*. Washington, DC: USACE.

Briaud, J. L., A. V. Govindasamy, and I. Shafii. 2017. "Erosion charts for selected geomaterials." *J. Geotech. Geoenviron. Eng.* 143 (10): 1–13. https://doi.org/10.1061/(ASCE)GT.1943-5606.0001771.

DeHaan, H., J. Stamper, and B. Walters. 2012. *Mississippi River and tributaries system 2011 post-flood report*. Vicksburg, MS: USACE.

de Wit, J. M. 1984. *Onderzoek zandmeevoerende wellen Rapportage Modelproeven*. Rep. No. CO-220885/10. Delft, Netherlands: Grondmechanica Delft.

Ferreira, T., and W. Rasband. 2012. "ImageJ User Guide, version IJ 1.46r." Accessed August 25, 2019. https://imagej.nih.gov/ij/docs/index.html.

Foster, M., R. Fell, and M. Spannagle. 2000. "The statistics of embankment dam failures and accidents." *Can. Geotech. J.* 37 (5): 1000–1024. https://doi.org/10.1139/t00-030.

Hoffmans, G., and L. Van Rijn. 2018. "Hydraulic approach for predicting piping in dikes." *J. Hydraul. Res.* 56 (2): 268–281. https://doi.org/10.1080/00221686.2017.1315747.

Kézdi, R. 1979. Vol. 25 of *Soil physics: Selected topics*. Amsterdam, Netherlands: Elsevier.

Knoeff, J. G., V. M. van Beek, and U. Förster. 2010. "Observations of piping on the IJkdijk test dike in the Netherlands." In *Proc., European Working Group on Internal Erosion*. Granada, Spain: Universidad de Granada.

Montalvo-Bartolomei, A. M., J. F. López-Soto, I. J. Stephens, and B. A. Robbins. 2016. "Solutions for various obstacles encountered with laboratory piping tests." In *Proc., 17th Nordic Geotechnical Meeting*. Reykjavik, Iceland: Icelandic Geotechnical Society.

Pol, J. C., V. M. van Beek, W. Kanning, and S. N. Jonkman. 2019. "Progression rate of backward erosion piping in laboratory experiments and reliability analysis." In *Proc., 7th Int. Symp. on Geotechnical Safety and Risk*. Taipei, Taiwan: Geotechnical Safety Network.

Richards, K. S., and K. R. Reddy. 2007. "Critical appraisal of piping phenomena in earth dams." *Bull. Eng. Geol. Environ.* 66 (4): 381–402. https://doi.org/10.1007/s10064-007-0095-0.

Robbins, B. A., and D. V. Griffiths. 2018. "Modelling of backward erosion piping in two- and three-dimensional domains." In *Internal erosion in earth dams, dikes, and levees*, edited by S. Bonelli, C. Jommi, and D. Sterpi, 149–158. Cham, Switzerland: Springer.

Robbins, B. A., and V. M. van Beek. 2015. "Backward erosion piping: A historical review and discussion of influential factors." In *ASDSO dam safety*, 1–20. New Orleans: Association of State Dam Safety Officials.

Robbins, B. A., V. M. van Beek, J. Lopez-Soto, A. M. Montalvo-Bartolomei, and J. Murphy. 2018. "A novel laboratory test for backward erosion piping." *Int. J. Phys. Modell. Geotech.* 18 (5): 266–279. https://doi.org/10.1680/jphmg.17.00016.

Schaefer, J. A., T. M. O'Leary, and B. A. Robbins. 2017. "Assessing the implications of sand boils for backward erosion piping risk." In *Proc., Geo-Risk 2017: Geotechnical Risk Assessment and Management—GSP 285*. Reston, VA: ASCE. https://doi.org/10.1061/9780784480724.012.

Schmertmann, J. H. 2000. "The no-filter factor of safety against piping through sands." In *Judgement and innovation*, edited by F. Silva and E. Kavazanijian, Jr., 65–133. Reston, VA: ASCE.

Sellmeijer, J. B., and M. A. Koenders. 1991. "A mathematical model for piping." *Appl. Math. Modell.* 15 (11–12): 646–651. https://doi.org/10.1016/S0307-904X(09)81011-1.

Sellmeijer, J. B., J. Lopez de la Cruz, V. M. van Beek, and H. Knoeff. 2011. "Fine-tuning of the backward erosion piping model through small-scale, medium-scale, and IJkdijk experiments." *Eur. J. Environ. Civ. Eng.* 15 (8): 1139–1154. https://doi.org/10.1080/19648189.2011.9714845.

© ASCE 04020093-11 J. Geotech. Geoenviron. Eng.

J. Geotech. Geoenviron. Eng., 2020, 146(9): 04020093

Townsend, F. C., J. H. Schmertmann, T. J. Logan, T. J. Pietrus, and Y. W. Wong. 1981. *An analytical and experimental investigation of a quantitative theory for piping in sand*. Gainesville, FL: Dept. of Civil Engineering, College of Engineering, Univ. of Florida.

van Beek, V. M., A. Bezuijen, J. Sellmeijer, and F. B. J. Barends. 2014. "Initiation of backward erosion piping in uniform sands." *Géotechnique* 64 (12): 927–941. https://doi.org/10.1680/geot.13.P.210.

van Beek, V. M., B. A. Robbins, G. J. C. M. Hoffmans, A. Bezuijen, and L. C. van Rijn. 2019. "Use of incipient motion data for backward erosion piping models." *Int. J. Sediment Res.* 34 (5): 401–408. https://doi.org/10.1016/j.ijsrc.2019.03.001.

van Beek, V. M., H. van Knoeff, and H. Sellmeijer. 2011. "Observations on the process of backward erosion piping in small-, medium- and full-scale experiments." *Eur. J. Environ. Civ. Eng.* 15 (8): 1115–1137. https://doi.org/10.3166/EJECE.15.1115-1137.

Vandenboer, K., F. Celette, and A. Bezuijen. 2019. "The effect of sudden critical and supercritical hydraulic loads on backward erosion piping: Small-scale experiments." *Acta Geotech.* 14 (3): 783–794. https://doi.org/10.1007/s11440-018-0756-0.

Yao, Q. 2014. *Multi-size experiments and numerical simulation for backward erosion piping in dike foundations*. [In Chinese.] Beijing: China Institute of Water Resrouces and Hydropower Research.

© ASCE 04020093-12 J. Geotech. Geoenviron. Eng.

J. Geotech. Geoenviron. Eng., 2020, 146(9): 04020093